BATTERIES

Superionic lithium transport via multiple coordination environments defined by two-anion packing

Guopeng Han[1], Andrij Vasylenko[1], Luke M. Daniels[1], Chris M. Collins[1], Lucia Corti[1,2], Ruiyong Chen[1], Hongjun Niu[1], Troy D. Manning[1], Dmytro Antypov[1,2], Matthew S. Dyer[1,2], Jungwoo Lim[1,3], Marco Zanella[1], Manel Sonni[1], Mounib Bahri[4], Hongil Jo[1,2], Yun Dang[1], Craig M. Robertson[1], Frédéric Blanc[1,2,3], Laurence J. Hardwick[1,2,3], Nigel D. Browning[4,5], John B. Claridge[1,2]*, Matthew J. Rosseinsky[1,2]*

Fast cation transport in solids underpins energy storage. Materials design has focused on structures that can define transport pathways with minimal cation coordination change, restricting attention to a small part of chemical space. Motivated by the greater structural diversity of binary intermetallics than that of the metallic elements, we used two anions to build a pathway for three-dimensional superionic lithium ion conductivity that exploits multiple cation coordination environments. $Li_7Si_2S_7I$ is a pure lithium ion conductor created by an ordering of sulphide and iodide that combines elements of hexagonal and cubic close-packing analogously to the structure of NiZr. The resulting diverse network of lithium positions with distinct geometries and anion coordination chemistries affords low barriers to transport, opening a large structural space for high cation conductivity.

The discovery of high-performance inorganic crystalline solid-state lithium ion (Li^+) electrolytes remains a challenge to facilitate the development of next-generation battery technologies (1–3). The high ionic conductivity of solid electrolytes at room temperature is critical to cell performance to ensure a low cell resistance and a high loading of active materials in the cathode composite without competing electronic conductivity. In addition, good chemical compatibility between the solid electrolyte and Li metal is required, which would enable the use of a Li anode to afford greater energy densities (4). A small number of established structural families give rise to current state-of-the-art solid Li^+ ion conductors that exhibit ionic conductivities comparable with that of liquid electrolytes ($\approx 10^{-2}$ S cm^{-1}). Examples include $Li_{10}GeP_2S_{12}$ (5, 6), $Li_{6.6}Si_{0.6}Sb_{0.4}S_5I$ (7), and $Li_7P_3S_{11}$ (8). The structures of each of these families create transport paths that minimize changes in cation coordination, which has been suggested as the origin of their high conductivities (9–11). This has led to materials design that emphasizes anion packings that afford predominantly or solely a single type of Li coor-

dination environment, which restricts the available chemical space. Using a different design strategy that utilizes multiple anions to construct suitable pathways, we synthesized a material in which many different cation coordination environments combine to create superionic conductivity. This greatly expands the number and type of potential structures that can support high cation mobility.

The search for materials that define transport pathways with homogeneous cation coordination has emphasized the role of tetrahedral Li sites (12, 13). In particular, attention has focused on body-centered cubic (bcc) arrangements of anions, which enable the formation of percolating Li^+ pathways that consist of energetically equivalent face-sharing tetrahedral sites yielding low activation energies for migration (14–17). bcc-like anion arrangements, which are rare because of the low density that leads them to favor cation mobility, are adopted by high-performance Li^+ ion conductors such as $Li_{10}GeP_2S_{12}$ and $Li_7P_3S_{11}$ (14). The A_7TX_6 (where A = Li, Ag, or Cu; T = P; and X = S) argyrodite structure has a tetrahedrally close-packed anion arrangement (18–20) that produces solely tetrahedral interstitial sites. Although this fits the structure-property relationship proposed for high cation mobility, the tetrahedral close packing of the anions in argyrodite is that of the metals in intermetallic Laves phases such as $MgCu_2$ (Fig. 1A), which are known to exhibit many other properties of interest, including hydrogen uptake and mobility within the interstitial space (21, 22).

The anion arrangements that define the cation sites in other high-performance Li^+ ion conductors can also be closely related to known intermetallic nets. The anion sublattice

of $Li_{10}GeP_2S_{12}$ is related to the As net of CrAs (Fig. 1B) (5, 23). This is not limited to sulphides. The oxide anion framework of the Li ion-conducting garnet $Li_7La_3Zr_2O_{12}$ can be compared with the Bi framework of Bi_4Rh (Fig. 1C); here, La^{3+} occupies the same site as Rh (24, 25).

Anion packings with precedent in the structures of intermetallic compounds can thus generate mobility pathways that require minimal coordination change based on tetrahedral interstitial cation sites. Because several properties must be optimized to yield a viable electrolyte, it would be helpful to expand the potential materials design space to harness pathways exploiting the widest possible range of Li sites. The structural diversity of intermetallics, in which multiple elements with distinct chemistries take part in the sphere packing, describes a far wider range of interstitial environments that enable transport (26, 27). This raises the possibility of more complex anion packings that are based on intermetallics and do not rely on a single coordination geometry for Li mobility. A high Li mobility material may be considered as an anion packing supported by a localized framework-forming cationic species M that interacts covalently with the anions to provide chemical stability. Because intermetallics such as Ti_2Ni describe multiple interstitial sites with a range of coordination environments that enable hydrogen transport and uptake (28), we can envisage packing multiple anions in this way to generate transport pathways that connect diverse Li sites through low barriers (Fig. 1D). Discovery synthesis that explores the connection between the large structural space established for intermetallic bonding and the creation of an equivalent space in ionic materials then offers a route to expand the small number of parent structures that afford superionic conductivity by creating transport paths that feature the full range of Li coordination.

Results and discussion
Element selection and material synthesis

We targeted complex packings that tailor the coordination at multiple distinct interstitial cation sites to optimize transport by using the size and charge diversity offered by multiple anions to replicate the bonding diversity of intermetallics (Fig. 1D). This motivates the experimental exploration of quaternary phase fields defined by Li^+, a suitable cation-forming element M, and two anions (X and X'). Consideration of appropriate abundance, toxicity, and electronic structure restricts the unexplored Li-M-X-X' chemical space to 296 phase fields [supplementary materials (SM), materials and methods]. Our exact selection of elements from this set was informed by a variational autoencoder (VAE) (29). The VAE operates at the level of combinations of elements, encoded by their chemical characteristics. It is trained

[1]Department of Chemistry, University of Liverpool, Crown Street, Liverpool L69 7ZD, UK. [2]Leverhulme Research Centre for Functional Materials Design, Materials Innovation Factory, 51 Oxford Street, University of Liverpool, Liverpool L7 3NY, UK. [3]Stephenson Institute for Renewable Energy, University of Liverpool, Liverpool L69 7ZF, UK. [4]Albert Crewe Centre, University of Liverpool, Research Technology Building, Elisabeth Street, Pembroke Place, Liverpool L69 3GE, UK. [5]School of Engineering, Department of Mechanical, Materials and Aerospace Engineering, University of Liverpool, Liverpool L69 3GH, UK.
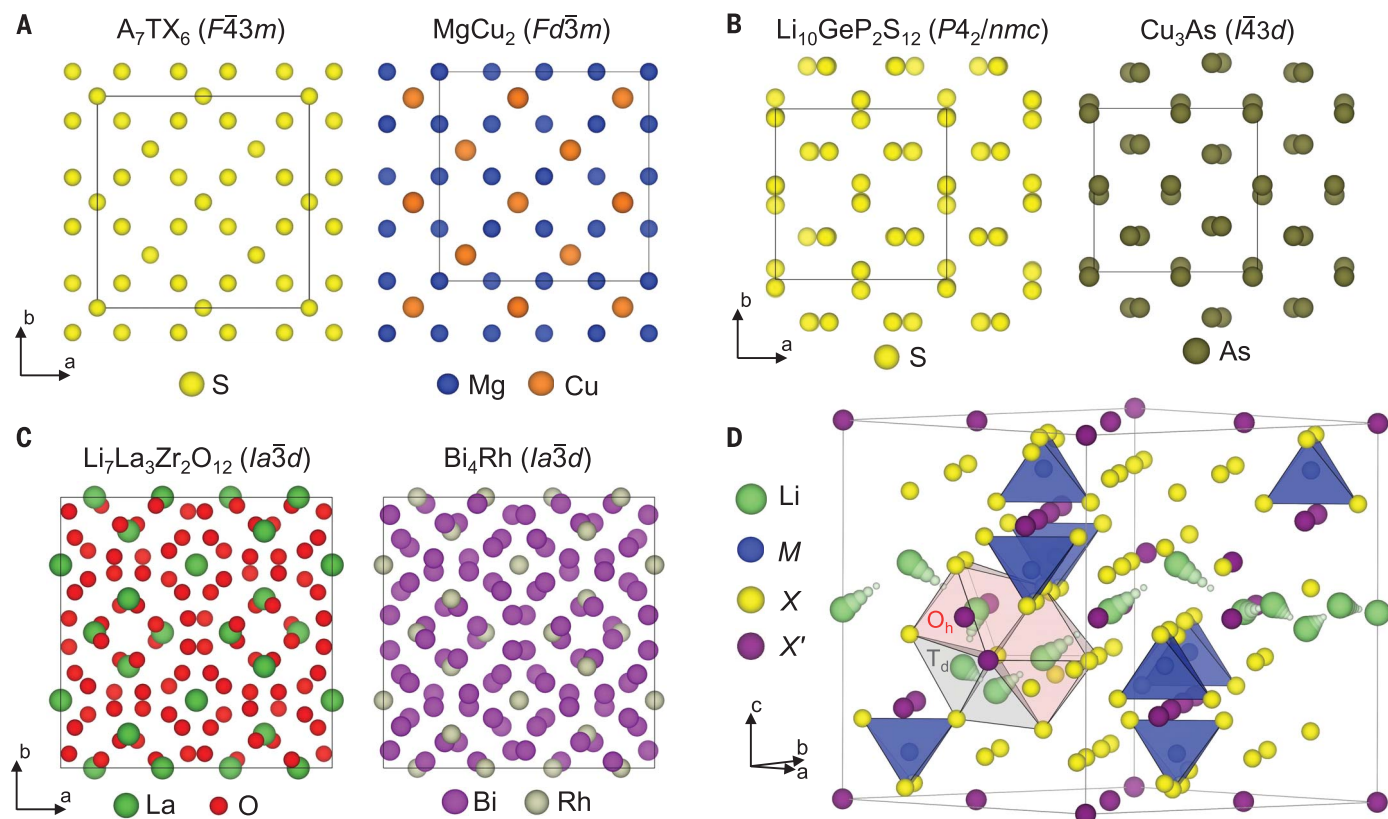*Corresponding author. Email: j.b.claridge@liverpool.ac.uk (J.B.C.); m.j.rosseinsky@liverpool.ac.uk (M.J.R.)

Fig. 1. Ionic conductors and intermetallic nets. (**A** to **C**) Comparison of the structures of high-performance Li$^+$ ion conductors with known intermetallic nets. (A) A$_7$TX$_6$ argyrodite and MgCu$_2$ Laves phase. (B) Li$_{10}$GeP$_2$S$_{12}$ and Cu$_3$As. (C) Li$_7$La$_3$Zr$_2$O$_{12}$ garnet and Bi$_4$Rh. (**D**) A conceptual view of the chemical components of a high Li mobility structure consisting of a framework-forming cation (M) and mobile Li$^+$ within a packing arrangement formed from two anions X and X'. This schematic is based on the packing in the binary intermetallic Ti$_2$Ni, with anions occupying the Ti and Ni positions, and highlights potential cation transport pathways that exploit multiple coordination environments.

to recognize patterns of similarity between 2021 synthetically accessible M-M'-X-X' phase fields reported as containing experimentally realized materials in (*30*) and, on the basis of the resulting latent space, quantitatively ranks unexplored chemistries according to their likelihood of containing new compounds. The VAE ranks Li-Si-S-Cl, Li-Si-S-Br, and Li-Si-S-I phase fields first, third, and ninth, respectively, within the selected chemical space, and we therefore selected Li-Si-S-halogen chemistry for exploration. Structural considerations focused attention on the Li-Si-S-I phase field that maximizes the difference in anion size [S^{2-} radius (*r*) = 1.84 Å versus Cl$^-$ *r* = 1.81 Å, Br$^-$ *r* = 1.95 Å, and I$^-$ *r* = 2.2 Å] and thus strengthens the connection to complex sphere packings driven by distinct structural roles of the anions involved, analogous to intermetallic binaries (*31*). The impact of using anions distinct in size and chemistry has been recently highlighted for Li- and Na-rich antiperovskites (*32, 33*). Computational exploration of the Li-Si-S-I phase field with probe structure prediction (*34–36*) indicates a synthetically accessible low-energy region of compositional space, which was targeted experimentally (fig. S1).

Solid-state syntheses for the compositions in this low-energy region were carried out in carbon crucibles inside evacuated fused silica ampoules, with the resulting phase assemblages identified with x-ray diffraction (XRD). These measurements indicated the formation of a phase that could not be matched to any known materials in the Li-Si-S-I field, and suitable crystals for single-crystal diffraction were grown by means of crystallization of Li$_2$S, LiI, and elemental Si from an elemental S flux (SM materials and methods). The crystal structure of a new phase, Li$_7$Si$_2$S$_7$I (LSSI), was solved in monoclinic *P*2$_1$/*n* symmetry by using high-resolution synchrotron single-crystal XRD data collected at beamline I19, Diamond Light Source (tables S2 to S6). Phase-pure powder samples of Li$_7$Si$_2$S$_7$I were synthesized by combining SiS$_2$, Li$_2$S, and LiI, using a 5% excess of SiS$_2$ that avoids formation of Li$_2$SiS$_3$ and Li$_4$SiS$_4$, and heating to 723 K for 4 days with 20 K min^{-1} heating rate and intermediate grinding after 2 days (SM materials and methods and figs. S2 to S5). Compositional analysis by means of CHNS (carbon-hydrogen-nitrogen-sulfur) and inductively coupled plasma (ICP) methods gave a mea-

sured composition of Li$_{6.9(2)}$Si$_{2.050(5)}$S$_{6.96(3)}$I$_{0.95(1)}$, which is consistent with Li$_7$Si$_2$S$_7$I determined from single-crystal XRD (table S7).

Crystal structure

The anion packing of Li$_7$Si$_2$S$_7$I can be connected to the TlI (B33)–type structures, such as the binary intermetallic NiZr (*37*). The intermetallic net in NiZr is intermediate between the well-known hexagonal and square nets (3^6 and 4^4 in Schläfli notation, respectively) and is a 3^3.4^2 semiregular net. A close-packed 3^6 layer is transformed by shearing every other row of triangles (Fig. 2A) to produce rows of triangles and quadrilaterals that alternate perpendicular to the shear direction (*38*). Every sphere in the resulting 3^3.4^2 layer is five-coordinate and takes part in three edge-sharing triangles and two edge-sharing quadrilaterals. In the anion packing of Li$_7$Si$_2$S$_7$I, S^{2-} and I$^-$ are ordered over the nodes of the 3^3.4^2 net (Fig. 2B), producing pure S^{2-} (S$_4$) and mixed S^{2-}/I$^-$ (S$_3$I) rows of spheres that run along the shear direction (the *c* axis) and alternate perpendicular to it in the *ac* plane.

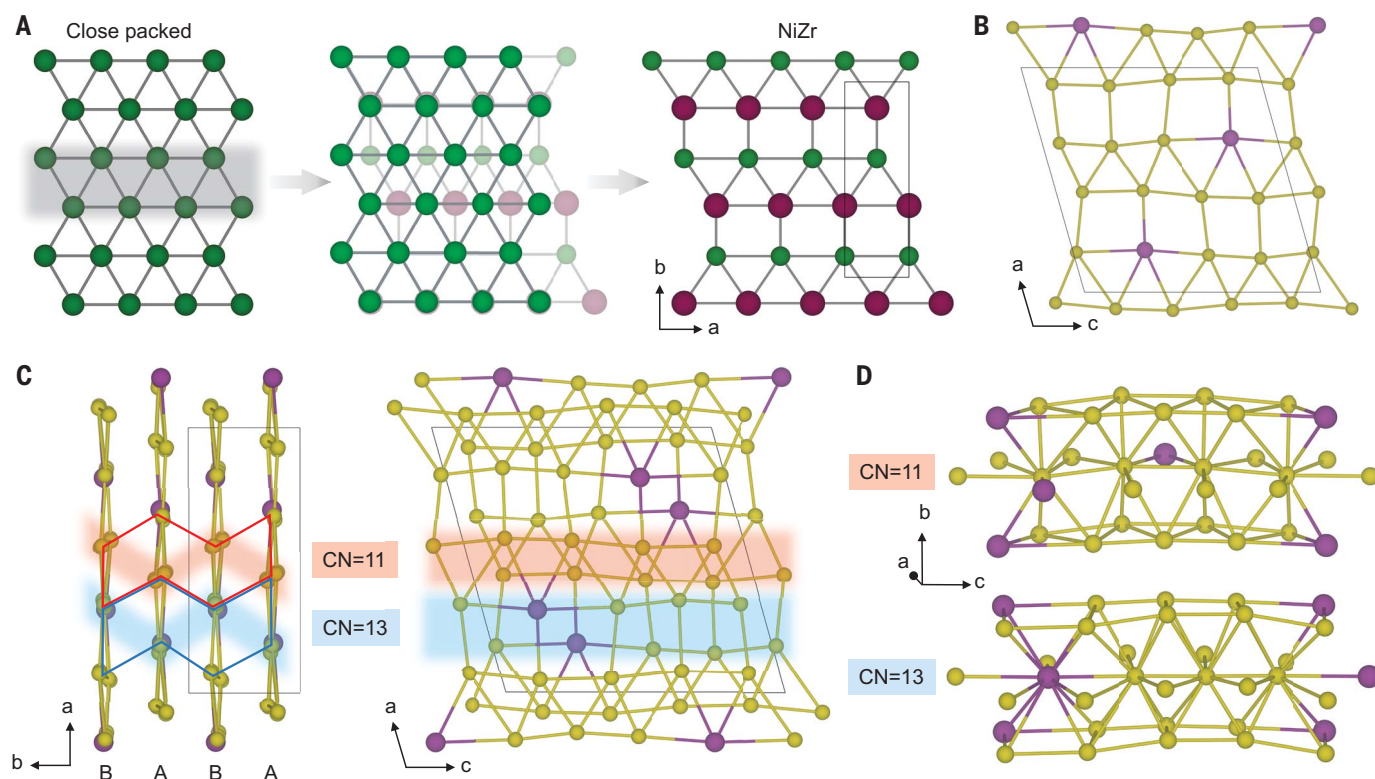These sheared layers stack in an ABAB sequence, similar to the hydride of NiZr (*39*) (fig. S6),

Fig. 2. Multiple anion order shears close-packed layers in Li₇Si₂S₇I.
(**A**) A single 3^6 close-packed layer is transformed into the $3^3.4^2$ semiregular net of NiZr by shearing every other row of triangles. Ni and Zr atoms are green and maroon, respectively. (**B**) Li₇Si₂S₇I has an anion topology based on NiZr, where S^{2-} (yellow) and I^- (purple) are ordered in $3^3.4^2$ layers. (**C**) ABAB stacking of these layers along b with resulting proximity of neighboring I^- anions produces (**D**) anion coordination spheres of 11 (S_4 rows) and 13 (S_3I rows) from superposition of triangles and quadrilaterals in neighboring layers, respectively. The CN = 11 (red shading) and CN = 13 (blue shading) rows are stacked along b in a zig-zag manner to form pairs in the bc plane that alternate along a. Four rows of anions with a 13-11-11-13 (S_3I-S_4-S_4-S_3I) CN sequence define hcp motifs [(C), left, solid red line] that alternate with sheared fcc-like motifs (solid blue line) defined by an 11-13-13-11 (S_4-S_3I-S_3I-S_4) sequence of anion rows.

along b that places each I^- between the centroids of S_3I quadrilaterals in both neighboring layers (Fig. 2C). This creates a 13-coordinate environment for the larger I^- that arises from the quadrilaterals produced by the shear. The quadrilaterals involved are the largest of the four in the unit cell and thus have an I^- vertex (table S8), creating two columns of neighboring I^- spheres along b (Fig. 2C). All of the spheres in the S_3I rows have a coordination number (CN) of 13. The stacking also places every sphere in the S_4 rows between the centroids of superimposed triangles in the neighboring layers in a CN of 11 (Fig. 2D and table S6). This creates CN = 11 S_4 and CN = 13 S_3I rows (Fig. 2C, red and blue shading, respectively) that stack alternately along a and also alternate between two positions along b in a zig-zag manner.

The resulting anion packing can be viewed as the alternation of [0001] hexagonal close-packed (hcp) motifs and sheared face-centered cubic (fcc) [001]-like motifs along a (fig. S7). The hcp motifs (Fig. 2C, red solid line) arise from the superposition of the triangles in next-nearest-neighbor layers and are defined by an S_3I-S_4-S_4-S_3I sequence of anion rows along a. The sheared fcc [001]-like motifs (Fig. 2C, blue solid line) are produced by superposition of the quadrilaterals generated by the shear and are defined by an S_4-S_3I-S_3I-S_4 sequence along a. The Li₇Si₂S₇I anion packing factor of 68.9% is higher than that of bcc-derived Li₁₀GeP₂S₁₂ (66.5%) and the tetrahedrally close-packed argyrodites (62.8% for Li₇PS₆ and 67.1% for Li₆PS₅I).

The NiZr intermetallic exhibits extensive H uptake (*39*), which reflects the large number of available interstitial sites generated by the packing of $3^3.4^2$ semiregular nets. Similarly, the anion topology in Li₇Si₂S₇I generates a diverse array of interstitial sites that emerge from the octahedral (O) and tetrahedral (T) geometries expected in simple close-packing (Fig. 3, A to E; fig. S8; and table S9). Within the hcp motif, the O_{hcp} sites share faces with each other along the triangle-stacking direction b, as do the T_{hcp} sites. In the shear-derived fcc-like motif, O_{fcc} and T_{fcc} sites share edges and corners, respectively, whereas O_{fcc} sites share faces with T_{fcc} neighbors (Fig. 3D). O_{hcp} and O_{fcc} sites, and T_{hcp} and T_{fcc} sites, share faces along a (fig. S9), which

combines the hcp and fcc-like motifs into the extended structure of Li₇Si₂S₇I.

Silicon was selected as part of the chemical space for experimental exploration because of its role in defining a stable anion framework through strong localized bonding. As the smallest cation present ($Si^{4+} r = 0.26$ Å, $Li^+ r = 0.59$ Å), Si^{4+} occupies the tetrahedral voids in the hcp layer that are solely coordinated by S^{2-}: $T1_{hcp}$, which is the smallest tetrahedral site in the structure and located far from the large I^- anions (table S10). The two occupied $T1_{hcp}$ sites ($T1a_{hcp}$) share corners to form Si_2S_7 dimers (Fig. 3, B to E).

The arrangement of Si^{4+} and I^- then directs the occupancy of the other sites by Li^+. The interstitial sites that share faces with the Si_2S_7 dimers are empty for electrostatic repulsion reasons (Fig. 3E and fig. S8). All four remaining T_{hcp} voids within the hcp motif have S_3I coordination ($T2_{hcp}$) and are partially occupied (between 9.8 and 50.3%) by Li^+. Of the remaining three O_{hcp} sites (tables S9 and S11), $O2_{hcp}$ with S_5I coordination is fully occupied by Li^+, whereas the two S_6-defined $O1_{hcp}$ sites accommodate three disordered Li^+ sites: one at the octahedron center and two S_4-coordinated positions displaced
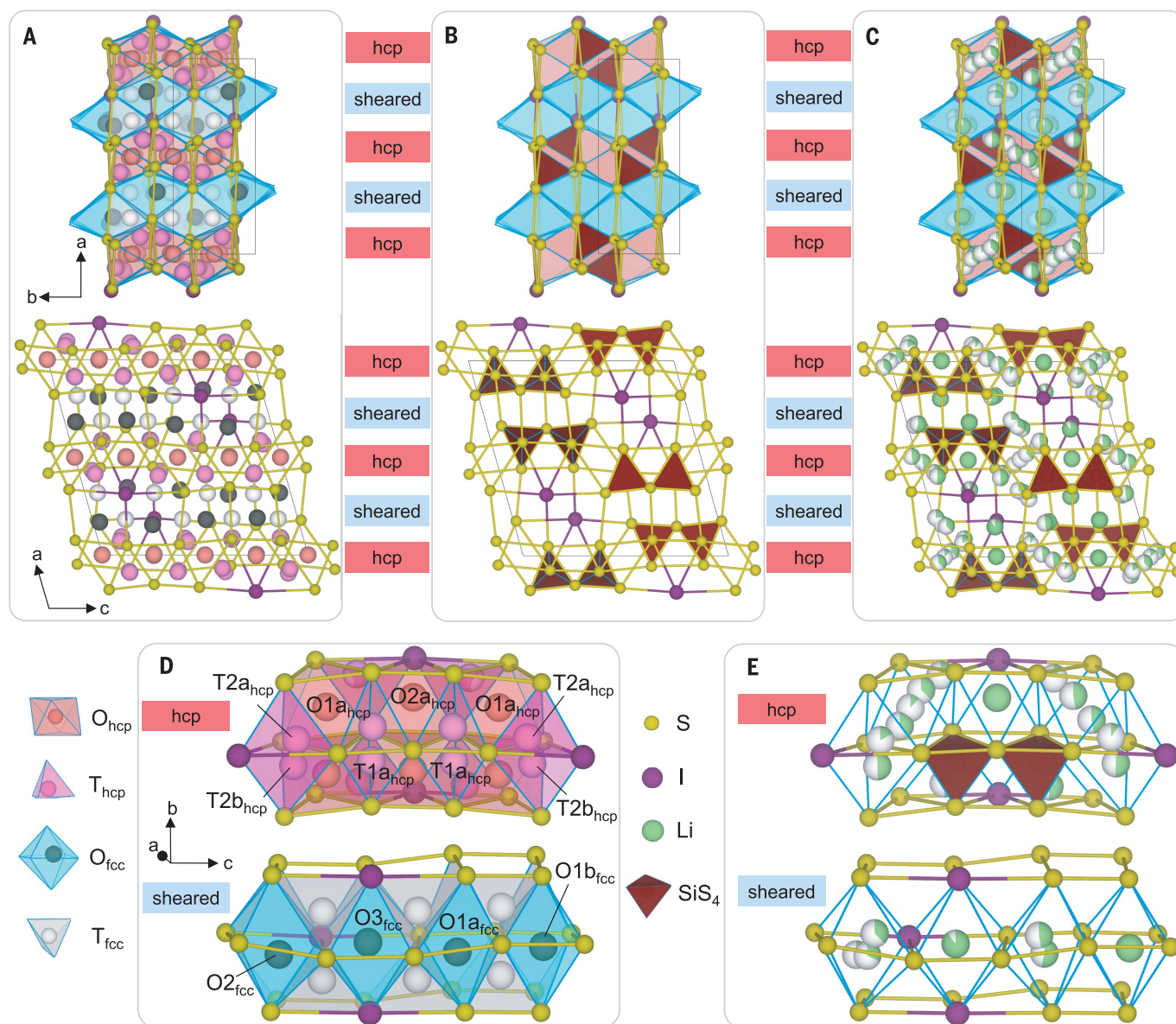
Fig. 3. Multiple coordination geometry interstitial sites and cation occupancy patterns in $Li_7Si_2S_7I$. (**A** to **C**) The unit cell of $Li_7Si_2S_7I$ viewed along c and b shows (A) the available interstitial sites, (B) the tetrahedral sites occupied by Si^{4+} to form Si_2S_7 dimers, and (C) the sites occupied by Si^{4+} and Li^+ (partial occupancy indicated by fraction of green shading). (**D**) The interstitial sites available for cation occupancy in the distinct hcp and sheared fcc-like anion motifs. (**E**) The sites occupied by Si^{4+} and Li^+ within $Li_7Si_2S_7I$. The interstitial sites are categorized according to their location (hcp or sheared fcc-like motifs),

the coordinating anions, and the connectivity to Si_2S_7 dimers (fig. S8 and table S9). The octahedral and tetrahedral sites (O_{hcp} and T_{hcp}) in the hcp motif are red and pink, respectively. The O_{fcc} and T_{fcc} sites in the sheared fcc-like motif are blue and gray, respectively. The two smallest corner-sharing tetrahedral sites formed solely by S^{2-} anions are within the hcp motif ($T1a_{hcp}$) and are occupied by Si^{4+}, forming Si_2S_7 dimers. The sites that share edges or corners with Si_2S_7 dimers are more favorable for Li^+ occupancy than those that share faces.

toward the triangular faces shared with two neighboring $T2_{hcp}$ sites (Fig. 3E). This forms chains of disordered, partially occupied Li^+ sites with short Li–Li distances in the range 0.943(12) to 1.34(3) Å (numbers in parentheses are estimated standard deviations from the refined structural model). All four types of octahedral site in the sheared layer are occupied by Li^+, whereas all eight tetrahedral sites are unoccupied; the two

with S_3I coordination, which is favored in the hcp motif, appear too small to accommodate Li in the sheared fcc-like motif (fig. S8 and table S10). Two of the octahedral sites ($O1a_{fcc}$ with S_6 coordination and $O2_{fcc}$ with S_5I coordination) accommodate more than one Li^+ position in a disordered manner (Fig. 3E). The mixed anion packing thus creates an interconnected set of 15 crystallographically distinct Li positions distributed across par-

tially occupied interstitial sites featuring extensive positional disorder over four-, five-, and six-coordinate geometries defined by varying anion coordination (tables S5 and S9). Although this site diversity, large unit cell, and low symmetry contrast strongly with current high-conductivity families, such a structure would be a strong candidate for high Li mobility if the wide site distribution implied a flat potential landscape.

Fig. 4. Ionic conductivity and stability of phase pure Li₇Si₂S₇I. (**A**) Temperature dependence of the total and bulk conductivity of $Li_7Si_2S_7I$, with derived activation energies shown. (Inset) Representative Nyquist plots between 303 and 373 K. The vertical and horizontal dashed lines highlight the room-temperature conductivity. (**B**) $Li_7Si_2S_7I$ undergoes an isostructural phase transition in which three of the Li^+ sites (gray spheres in the 240 K structure) observed at 300 K and above within the hcp motif become unoccupied at 240 K and below (fig. S13). The occupancies of all Li^+ sites in $Li_7Si_2S_7I$ between 100 and 500 K are summarized in table S12. (**C**) Galvanostatic Li plating and stripping voltage profiles of a symmetrical $Li|Li_7Si_2S_7I|$ Li cell measured at 303 K with 0.05 mA cm⁻² for 120 hours and then at 0.1 mA cm⁻² for a further 120 hours. This is measured on a phase-pure sample, not a composite with impurity phases. (**D**) Full width at half maximum of the static ⁷Li central NMR transition Δν (black squares) as a function of temperature fitted to a Boltzmann sigmoid regression curve (gray line), highlighting the low onset temperature of line narrowing (orange line) at $T_{onset} \sim 179$ K. (**E**) ⁷Li spin lattice relaxation rates in the laboratory frame T_1 (black diamonds) and rotating frame $T_{1\rho}$ at different spin-lock frequencies (colored diamonds) as a function of reciprocal temperature modeled as discussed in the SM (only the

fit to the data obtained with ν₁ of 80 kHz is shown for clarity; blue dashed and solid lines indicate the individual and overall processes, respectively) to extract the activation barriers. The dashed vertical line at 295 K indicates the discontinuity in slopes observed in the rates.
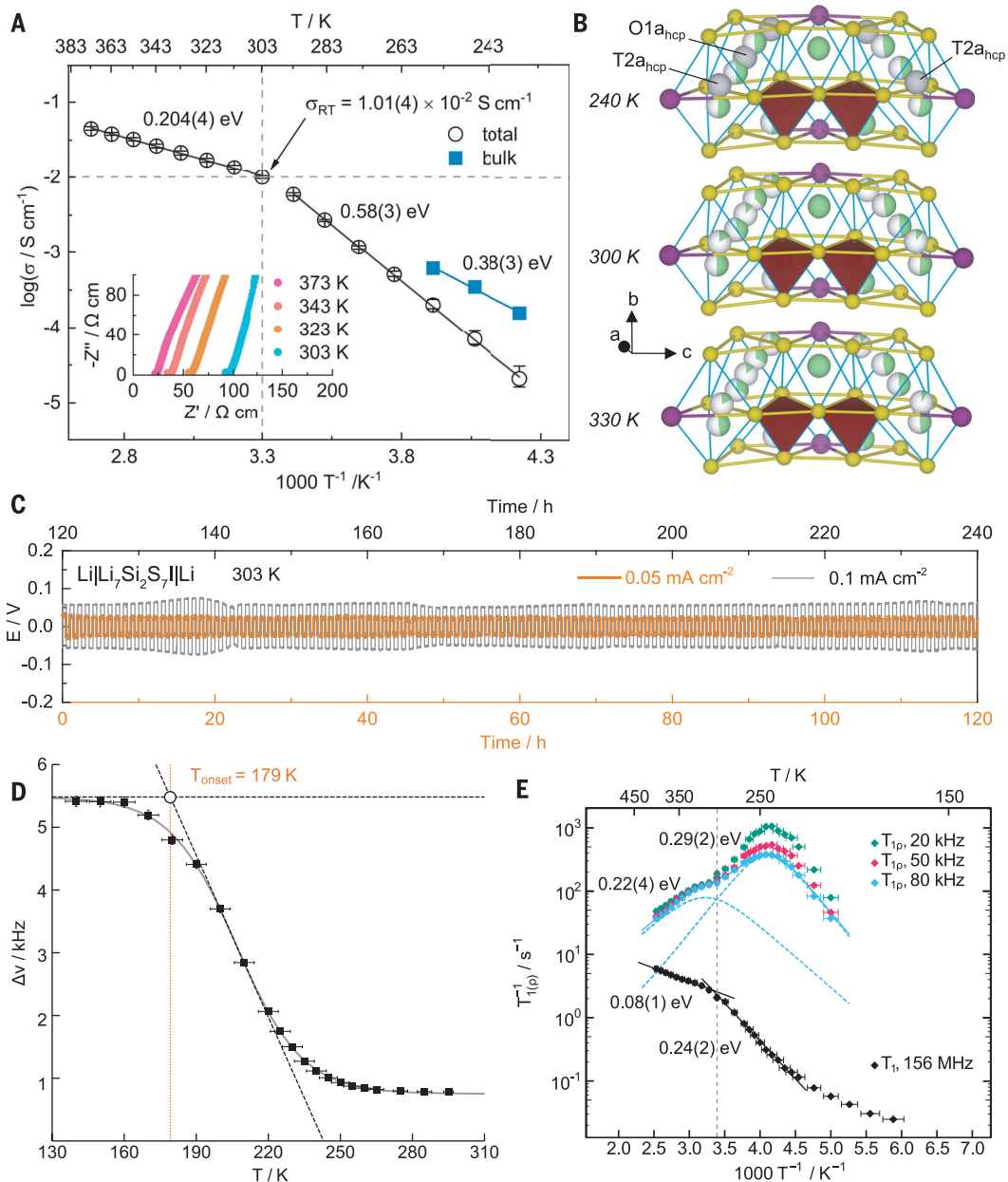
Transport properties

Alternating current (ac) impedance measurements on sintered pellets with blocking Au electrodes show that phase-pure $Li_7Si_2S_7I$ has a total conductivity of $1.01(4) \times 10^{-2}$ S cm⁻¹ at 303 K (Fig. 4A). The electronic contribution to the total conductivity is negligible ($\approx10^{-10}$ S cm⁻¹, measured with direct-current polarization) (fig. S11). The Arrhenius plots (Fig. 4A and fig. S12) show two temperature ranges with different activation energies for the conductivity: 0.204(4) eV for the total conductivity between 303 and 373 K, and 0.58(3) eV for the total, and 0.38(3) eV for the bulk conductivity between 237 and 293 K.

The activation energy of 0.204(4) eV is comparable with the lowest observed (0.20 to 0.34 eV) for argyrodite and $Li_{10}GeP_2S_{12}$ solid electrolytes (5, 40, 41). The structural transition (Fig. 4B and figs. S13 and S14) that depopulates two S_3I-defined tetrahedral and one S_6-defined octahedral Li^+ sites within the hcp motif of $Li_7Si_2S_7I$ between 237 and 293 K is associated with the reduced ionic conductivity and increased activation energy, which is consistent with coordination environment diversity enabling high mobility.

During linear sweep voltammetry measurements, no substantial reaction currents were detected within 10 V versus Li⁺/Li in a "stain-

less steel (SS)|$Li_7Si_2S_7I$|Li" configuration (fig. S15B, red curve). An oxidative decomposition potential of 2.5 V versus Li⁺/Li was observed for $Li_7Si_2S_7I$ (fig. S15B, black curve) when using a "$Li_7Si_2S_7I$ + carbon fiber (CF)|$Li_7Si_2S_7I$|Li" configuration. We observed steady Li plating and stripping on a $Li|Li_7Si_2S_7I|$Li cell over 240 hours at 0.05 and 0.1 mA cm⁻² (Fig. 4C), indicating a reasonably stable $Li_7Si_2S_7I$|Li interface (figs. S16 to S18). Stable cycling of $Li_7Si_2S_7I$ as the solid electrolyte within an all-solid-state cell was demonstrated against both the Li anode and $LiCoO_2$ cathode (fig. S19). The excellent Li transport properties were further
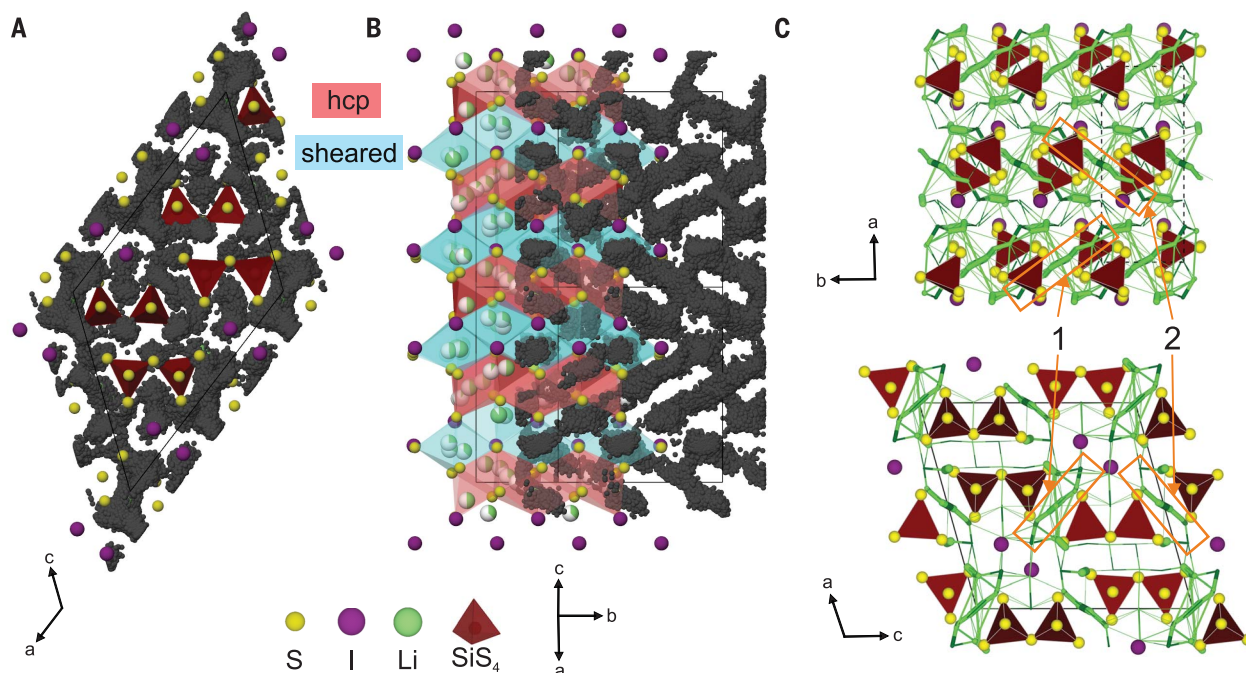
Fig. 5. AIMD simulation of Li₇Si₂S₇I. (**A** and **B**) Projections along the (A) [010] and (B) [101] directions of the $P2_1/c$ AIMD supercell, equivalent to the [010] and [001] directions in the experimental $P2_1/n$ unit cell shown in Fig. 3C (SM materials and methods). The black points indicate the calculated positions of Li atoms taken at time intervals of 0.05 ps from the 300-ps AIMD simulation at 500 K. The experimental structure at 300 K is overlaid with the simulation to guide the eye to the location of the hcp and sheared fcc–like motifs in the structure. The distribution of Li atoms in the simulation supports the experimental observation that Li⁺ is highly mobile in three dimensions. (**C**) Migration pathways through Li₇Si₂S₇I displayed as cylinders between occupied Li (green) and available interstitial sites (dark green) in the experimental structure at 300 K. The cross section of each cylinder is proportional to the hopping frequency observed in the AIMD simulation (fig. S26). The labeled orange boxes indicate the location of the two fast diffusion units 1 and 2 oriented in different directions within the structure. 3D transport between these units occurs through multiple connections with calculated activation barriers of 0.2 to 0.3 eV (fig. S29).

demonstrated by the low temperature (T_{onset} of ~179 K; below the temperature at which the total conductivity decreases) of the ⁷Li nuclear magnetic resonance (NMR) line narrowing (Fig. 4D), which is comparable with that of the fast Li⁺ ion conductors within the structural families discussed above (42–44). Modeling of the diffusion-induced ⁷Li spin lattice relaxation rate behaviors (Fig. 4E), as described in the SM materials and methods, captures both short- and long-range Li⁺ bulk ion transport in Li₇Si₂S₇I and also determines two different activation energies in the same temperature ranges as the conductivity measurements: 0.24(2) and 0.08(1) eV below and above ~295 K, respectively, for short-range Li⁺ ion mobility (Fig. 4E, black data) and 0.29(2) eV [comparable with the bulk conductivity value of 0.38(3) eV measured with ac impedance at low temperature] and 0.22(4) eV below and above ~295 K respectively for long range Li⁺ ion mobility (Fig. 4E, colored data). Critically, the ⁷Li spin lattice relaxation rates in the rotating frame $T_{1\rho}^{-1}$ are independent of the spin-lock frequencies on the high-temperature flank of the relaxation data (Fig. 4E, colored data above ~295 K) (45, 46), which is strong experimental evidence for three-dimensional (3D) long-range Li⁺ transport in Li₇Si₂S₇I.

Ion transport mechanism

In contrast with the three tetrahedral and one trigonal bipyramidal environments in highly conductive argyrodites (47), and the three tetrahedral and one octahedral environments in Li₁₀GeP₂S₁₂ (48), Li₇Si₂S₇I has substantially more Li⁺ site diversity arising from the structure-defining Si₂S₇ and I⁻ components. The 15 distinct Li⁺ positions in Li₇Si₂S₇I are located on S₃I tetrahedral and S₃I₃, S₅I, and S₆ octahedral interstitial sites and correspond to 10 different local modes of coordination (table S9). Ab initio molecular dynamics (AIMD) simulations were performed on Li₇Si₂S₇I at 400, 450, and 500 K (SM materials and methods) to identify transport paths and the associated free-energy landscape (fig. S29). These simulations demonstrate that all 15 occupied and 12 out of 13 available Li⁺ sites participate in ion transport (Fig. 5 and tables S15 to S17). Among the 162 distinct site-to-site connections observed to contribute to Li transport, there were 11 low-barrier (<0.2 eV) connections enabling rapid ionic motion within distinct units (Fig. 5C and fig. S29), with 3D transport established between these units and all the remaining Li sites through an additional 18 connections with absolute barriers of 0.2 to 0.3 eV (figs. S27 to S30). The arising vast array of migration options generated by the mul-

tiple low-barrier connections between the large number of chemically distinct accessible sites enables the fast transport observed in the complex, low-symmetry structure of Li₇Si₂S₇I. The theoretical activation energy for Li⁺ transport in Li₇Si₂S₇I of 0.16(1) eV extracted from the mean squared displacements across 400 to 500 K simulations (fig. S22C) agrees with experimentally measured values from impedance and NMR. Using eqs. S1 to S4 in the SM and the parameters fitted in fig. S22D, we obtained a calculated bulk ionic conductivity extrapolated to 300 K of 0.023(9) S cm⁻¹, which is in good agreement with the experimentally observed value. The calculated diffusion coefficients along the crystallographic axes lie within a factor of two (fig. S22, A and B), which is consistent with 3D transport observed with NMR (Fig. 4E).

Conclusions

Li₇Si₂S₇I (LSSI) has 3D interconnected pathways for cation mobility, linking multiple partially occupied Li⁺ sites of distinct geometry, anion coordination, and size with low barriers to ion transport. The high room-temperature Li⁺ ion conductivity of $1.01(4) \times 10^{-2}$ S cm⁻¹ is combined with low electronic conductivity and compatibility with a Li metal anode. Many optimization strategies to enhance desirable

combinations of these properties are available, such as the introduction of anion disorder and the suppression by substitution of the structural phase transition that occurs just below room temperature. The potential to implement such strategies is facilitated by the structural diversity of the material, with many distinct sites to target chemically.

The anion topology of $Li_7Si_2S_7I$ blends hexagonal and sheared cubic-like close-packing motifs to accommodate the distinct chemistries of sulphide and iodide. The high conductivity arises from a combination of Li^+ sites of widely varying geometry and anion coordination, in contrast to design strategies that focus on minimizing cation coordination change. Rather than restricting design to realizing only those anion packings that can create conduction pathways where coordination geometry change is minimal, we can exploit the full range of Li coordination geometries by identifying the anion arrangements required to use them effectively for transport by accommodating the variations in bonding over the pathway. Diverse coordination environments in large, low-symmetry cells can be tailored to create partially occupied sites of equivalent energy, offering an alternative to disorder created by high symmetry. Drawing on the vast compositional and structural diversity of the intermetallics, $Li_7Si_2S_7I$ demonstrates the opportunities for superionic cation mobility in the rich design space of multiple anion packings directed by framework-forming elements that afford strong covalent bonds. The extensive site diversity produces many different low-barrier site-to-site connections, affording multiple rapid transport pathways. Such materials are accessible through the design principles described in Fig. 1D that are well suited to exploratory synthesis. The arising structures can readily be evaluated for potential cation mobility by considering the site distributions within them and computationally identifying low-barrier paths between these sites.

REFERENCES AND NOTES

1. A. Kondori et al., Science 379, 499–505 (2023).
2. Z. Ning et al., Nat. Mater. 20, 1121–1129 (2021).
3. F. Marchini et al., Adv. Energy Mater. 11, 2101111 (2021).
4. A. M. Abakumov, S. S. Fedotov, E. V. Antipov, J.-M. Tarascon, Nat. Commun. 11, 4976 (2020).
5. N. Kamaya et al., Nat. Mater. 10, 682–686 (2011).
6. J. A. Dawson, M. S. Islam, ACS Mater. Lett. 4, 424–431 (2022).
7. L. Zhou, N. Minafra, W. G. Zeier, L. F. Nazar, Acc. Chem. Res. 54, 2717–2728 (2021).
8. H. Yamane et al., Solid State Ion. 178, 1163–1167 (2007).
9. R. D. Armstrong, R. S. Bulmer, T. Dickinson, J. Solid State Chem. 8, 219–228 (1973).
10. J. C. Bachman et al., Chem. Rev. 116, 140–162 (2016).
11. Q. Zhang et al., Adv. Mater. 31, 1901131 (2019).
12. H. Fang, P. Jena, Nat. Commun. 13, 2078 (2022).
13. Y. Zeng et al., Science 378, 1320–1324 (2022).
14. Y. Wang et al., Nat. Mater. 14, 1026–1031 (2015).
15. A. Y. S. Eng et al., Sci. Adv. 8, eabm2422 (2022).
16. A. Banik et al., Chem. Sci. 12, 6238–6263 (2021).
17. S. P. Culver, R. Koerver, T. Krauskopf, W. G. Zeier, Chem. Mater. 30, 4179–4192 (2018).
18. W. F. Kuhs, R. Nitsche, K. Scheunemann, Mater. Res. Bull. 14, 241–248 (1979).
19. S.-T. Kong et al., Chem. Eur. J. 16, 2198–2206 (2010).
20. B. J. Morgan, Chem. Mater. 33, 2004–2018 (2021).
21. R. L. Berry, G. V. Raynor, Acta Crystallogr. 6, 178–186 (1953).
22. D. Ivey, D. Northwood, J. Less Common Met. 115, 23–33 (1986).
23. J. E. Iglesias, W. Nowacki, Z. Kristallogr. Cryst. Mater. 145, 334–345 (1977).
24. C. A. Geiger et al., Inorg. Chem. 50, 1089–1097 (2011).
25. R. G. Ross, W. Hume-Rothery, J. Less Common Met. 1, 304–308 (1959).
26. M. Hirscher et al., J. Alloys Compd. 827, 153548 (2020).
27. T. G. Akhmetshina, V. A. Blatov, D. M. Proserpio, A. P. Shevchenko, Acc. Chem. Res. 51, 21–30 (2018).
28. H. Buchner, M. A. Gutjahr, K.-D. Beccu, H. Säufferer, Int. J. Mater. Res. 63, 497–500 (1972).
29. A. Vasylenko et al., Nat. Commun. 12, 5561 (2021).
30. D. Zagorac, H. Müller, S. Ruehl, J. Zagorac, S. Rehme, J. Appl. Crystallogr. 52, 918–925 (2019).
31. R. D. Shannon, Acta Crystallogr. A 32, 751–767 (1976).
32. K. Kim, D. J. Siegel, J. Mater. Chem. A 7, 3216–3227 (2019).
33. P.-C. Tsai et al., Adv. Energy Mater. 13, 2203284 (2023).
34. C. M. Collins et al., Angew. Chem. Int. Ed. 60, 16457–16465 (2021).
35. C. Collins et al., Nature 546, 280–284 (2017).
36. D. C. Lonie, E. Zurek, Comput. Phys. Commun. 182, 372–387 (2011).
37. M. E. Kirkpatrick, D. M. Bailey, J. F. Smith, Acta Crystallogr. 15, 252–255 (1962).
38. M. O'Keeffe, B. G. Hyde, Philos. Trans. R. Soc. A 295, 553–623 (1980).
39. D. G. Westlake, J. Less Common Met. 75, 177–185 (1980).
40. P. Adeli et al., Angew. Chem. Int. Ed. 58, 8681–8686 (2019).
41. Y. Kato et al., Nat. Energy 1, 16030 (2016).
42. V. Epp, Ö. Gün, H.-J. Deiseroth, M. Wilkening, J. Phys. Chem. Lett. 4, 2118–2123 (2013).
43. A. Kuhn, V. Duppel, B. V. Lotsch, Energy Environ. Sci. 6, 3548–3552 (2013).
44. D. Wohlmuth, V. Epp, M. Wilkening, ChemPhysChem 16, 2582–2593 (2015).
45. C. A. Sholl, J. Phys. C Solid State Phys. 14, 447–464 (1981).
46. A. Kuhn et al., J. Am. Chem. Soc. 133, 11018–11021 (2011).
47. L. Zhou, A. Assoud, Q. Zhang, X. Wu, L. F. Nazar, J. Am. Chem. Soc. 141, 19002–19013 (2019).
48. A. Kuhn, J. Köhler, B. V. Lotsch, Phys. Chem. Chem. Phys. 15, 11620–11622 (2013).
49. K. Momma, F. Izumi, J. Appl. Crystallogr. 44, 1272–1276 (2011).
50. G. Han et al., Data for: Superionic lithium transport via multiple coordination environments defined by two anion packing. Datacat (2024); 10.17638/datacat.liverpool.ac.uk/1989.

SUPPLEMENTARY MATERIALS

science.org/doi/10.1126/science.adh5115
Materials and Methods
Supplementary Text
Figs. S1 to S30
Tables S1 to S17
References (51–104)
Data S1